ORIGINAL RESEARCH ARTICLE

Dendrite Growth in Single-Grain and Cyclic-Twinned Sn–3Ag–0.5Cu Solder Joints

S. SUN and C.M. GOURLAY

The microstructure of electronic solder joints is generated by the solidification of a small volume of bulk undercooled liquid. Here, we study β-Sn dendrite growth in Sn–3Ag–0.5Cu in the specific geometry and nucleation conditions of ball grid array (BGA) solder joints by combining electron backscatter diffraction and imaging of microstructures. It is shown that, while $\langle 110 \rangle$ is the preferred dendrite growth direction, out-of-plane branching and growth with $\langle 11W \rangle$ directions are important for allowing dendrites to fan out into the spheroidal volume of BGA joints due to the low symmetry of β-Sn. We find that the crystallographic orientation of β-Sn at the nucleation point plays a strong role in subsequent dendrite growth. In single-grain joints, dendrites are often unfavorably oriented for growth, resulting in different types of zig-zag dendrite growth. In cyclic-twinned joints, it is shown how competitive out-of-plane trunk growth between three dendrite orientations produces {101} boundaries and the characteristic beachball microstructure.

https://doi.org/10.1007/s11661-024-07580-9

I. INTRODUCTION

ELECTRONIC solder joints are typically sub-millimeter Sn-based alloys whose microstructure initially formed by solidification in an undercooled melt. A feature of Cu/Sn–Ag–Cu/Cu ball grid array (BGA) joints is the occurrence of a single β-Sn nucleation event during solidification,[1] typically on one of the Cu_6Sn_5 reaction layers,[2] leading to a single-grain or cyclic-twinned microstructure.[1] For example, Figure 1 shows typical solder microstructures in an 84 thin chip array BGA package using electron backscatter diffraction (EBSD) mapping of β-Sn orientations, highlighting the single-grain and multi-grain cyclic-twinned β-Sn grain structures. In the cyclic-twinned joint, the three β-Sn grain orientations are interrelated by ~ 60 deg rotations around the circled common $\langle 100 \rangle$ axis. The resulting "beachball" microstructure is widespread in BGA solder joints and has been reported by many groups[3–12] and linked to the nucleation stage by Lehman *et al.*[1]. In single-grain and beachball Sn–3Ag–0.5Cu microstructures, typically more than 50 pct of the volume is occupied by β-Sn dendrites. Lehman *et al.*[1] deduced that beachball microstructures typically contain six segments separated by irregular grain boundaries, and are created by the growth of β-Sn dendrites with three cyclic-twinned orientations that formed at or near the nucleation stage. However, there remain unresolved questions on the detail of how β-Sn dendrite growth and branching generate the beachball microstructure. Since the microstructure plays an important role in the reliability of electronics,[13,14] there is a need to better understand β-Sn dendrite growth in BGA solidification and its role in generating the beachball microstructure.

Past work has shown that the dominant dendrite growth directions in tetragonal β-Sn are usually $\langle 110 \rangle$.[15,16] Warner and Verhoeven found that β-Sn dendrites also fan out with subbranches that deviate from the $\langle 110 \rangle$ growth direction toward $\langle 001 \rangle$ with small angles in their Sn-2 wt pct Ag alloy.[16] A growth direction 12 deg away from $\langle 110 \rangle$ toward $\langle 001 \rangle$ (approximately $\langle 221 \rangle$) was also reported by two other groups[17–19] and "slight growth" in the [001] direction was reported by Weinberg and Chalmers.[15] As shown in Figure 1(g), in tetragonal β-Sn, the four $\langle 110 \rangle$ directions all lie in the single {001} plane and, therefore, $\langle 110 \rangle$ dendrite growth would be confined to one plane. In contrast, there are eight $\langle 221 \rangle$ directions, all with an out-of-plane component. However, each of them is only ~ 12 deg from the closest $\langle 110 \rangle$ and, thus, $\langle 221 \rangle$ growth is still not far from in-plane growth.

Most work on β-Sn dendrite growth has been in controlled solidification experiments. For example, with the Bridgman method[20,21] or other directional solidification methods,[17,22–25] there are typically numerous β-Sn orientations at the start of growth which compete

S. SUN and C.M. GOURLAY are with the Department of Materials, Imperial College London, London SW7 2AZ, UK. Contact e-mail: sihan.sun16@imperial.ac.uk
Manuscript submitted July 1, 2024; accepted August 23, 2024.
Article published online September 16, 2024

until dendrites that are well-oriented for growth are naturally selected. Less attention has been given to β-Sn dendrite growth in the specific geometry and nucleation conditions of a BGA solder joint, *i.e.*, in a sample with spheroidal shape where a single nucleation event occurs in a bulk undercooled melt at one point on/near the surface, typically at the L-Cu_6Sn_5 interface on one of the reaction layers.[2]

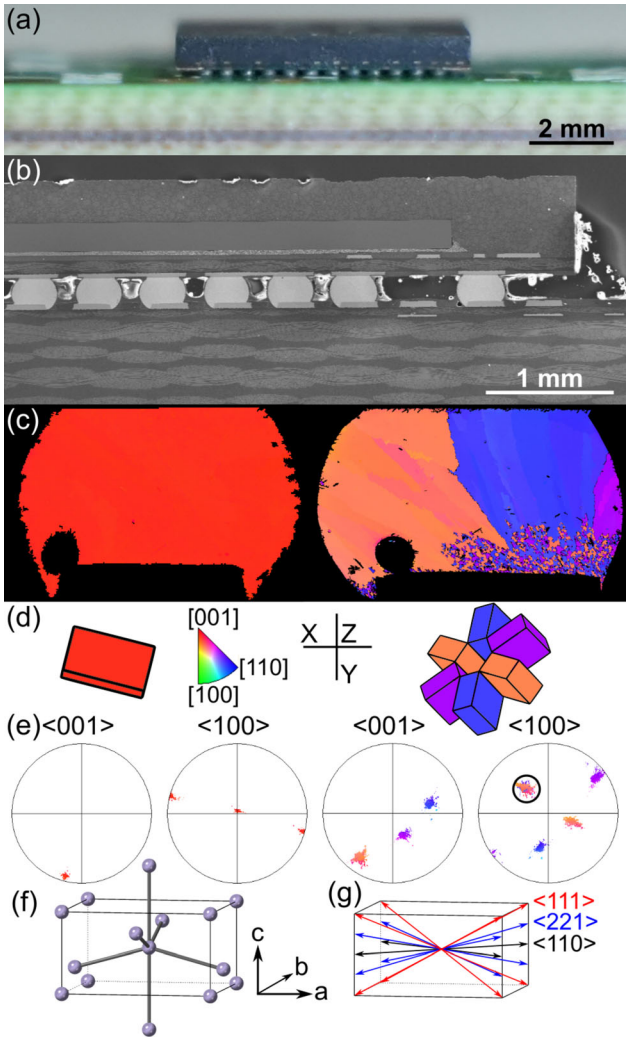

Fig. 1—Typical BGA solder joints connecting an electronic component to a printed circuit board. (*a*) A photograph of a soldered 84CTBGA package. (*b*) SEM image of a cross section containing the solder joints. (*c*) through (*e*) EBSD analysis of joints with single-grain (left) and cyclic-twinned (right) β-Sn grain structures. (c) Orientation maps with IPF-Y coloring. (d) Unit cell wireframes of β-Sn grains. (e) $\langle 001 \rangle$ and $\langle 100 \rangle$ pole figures. The black circle indicates a $\langle 100 \rangle$ axis shared by all three orientations. (*f*) Unit cell of tetragonal β-Sn. (*g*) Wireframe showing the $\langle 110 \rangle$ (black), $\langle 221 \rangle$ (blue), and $\langle 111 \rangle$ (red) directions (Color figure online).

This paper studies β-Sn dendrite growth in the specific case of Sn–3Ag–0.5Cu solidification in a BGA joint geometry with a focus on the following questions: How do β-Sn dendrites fill the 3D volume from their near-in-plane $\langle 110 \rangle$ and ~ $\langle 221 \rangle$ growth directions? How does the orientation of the β-Sn grain(s) at the nucleation site affect subsequent dendrite growth? And how does competitive dendrite growth produce the beachball microstructure in cyclic-twinned joints containing three orientations?

II. METHODS

This work involved individual Sn–3.0 wt pct Ag–0.5 wt pct Cu (SAC305) balls soldered onto a printed circuit board (PCB) producing half BGA joints. SAC305 balls of approximately 500 μm diameter were produced from ingots with composition in Table I by rolling them into foils, punching them into disks, and then melting them on a hot plate at 270 °C with a ROL1-type flux (IPC J-STD-004). Solder balls were placed on PCBs with 0.5 mm diameter copper pads coated in organic solderability preservative (OSP) with some ROL1 flux, and were melted and solidified in a LFR400HTX TORNADO reflow oven (Surface Mount Technology, Isle of Wight, UK) to form a ball grid array. The thermal profile involved heating at ~ 2 K/s to a peak temperature of ~ 250 °C and cooling at ~ 3 K/s to room temperature. Afterward, the solder joints were cleaned in an ultrasonic bath of ethanol for 10 minutes to remove the flux residue.

A second series of experiments was conducted in a differential scanning calorimeter (Mettler Toledo DSC1) to solidify SAC305 solder joints at a constant imposed cooling rate and measure the β-Sn nucleation temperature. Single solder joints with approximately 3 mm × 3 mm of PCB were cut out from the ball grid array with a guillotine cutter to fit into a DSC pan. The solder joints were then remelted in the DSC under a nitrogen atmosphere with a peak temperature of 240 °C and cooled at 20 K/min. For each joint, the nucleation undercooling was defined as the β-Sn liquidus temperature minus the onset temperature of the exothermic peak during cooling.

To prepare cross sections for characterization, Struers VersoCit-2 cold mounting acrylic resin was used before grinding with water on SiC foils with increasing grit

Table I. Composition of Sn–3Ag–0.5Cu in Wt Pct as Determined by XRF Spectroscopy

Ag	Cu	Pb	Sb	Bi	Zn	Fe	Al	As	Cd
3.052	0.504	0.029	0.007	0.003	< 0.001	0.003	< 0.001	< 0.001	< 0.001

numbers until 4000 grit. Next, they were polished with suspensions of 50 vol pct water and 50 vol pct OP-S NonDry colloidal silica suspension (Struers).

Optical micrographs and polarized optical micrographs of the solder joints were captured with an Olympus BX53M optical microscope equipped with a polarizer. A Zeiss Sigma 300 field emission gun scanning electron microscope (FEG–SEM) equipped with a Bruker eFlash HR electron backscatter diffraction (EBSD) detector was used to collect backscattered electron (BSE) micrographs and the EBSD maps. A Zeiss Auriga FEG–SEM was also used to acquire BSE micrographs with higher resolution when necessary. Bruker Esprit 2.1 was used for EBSD data analysis.

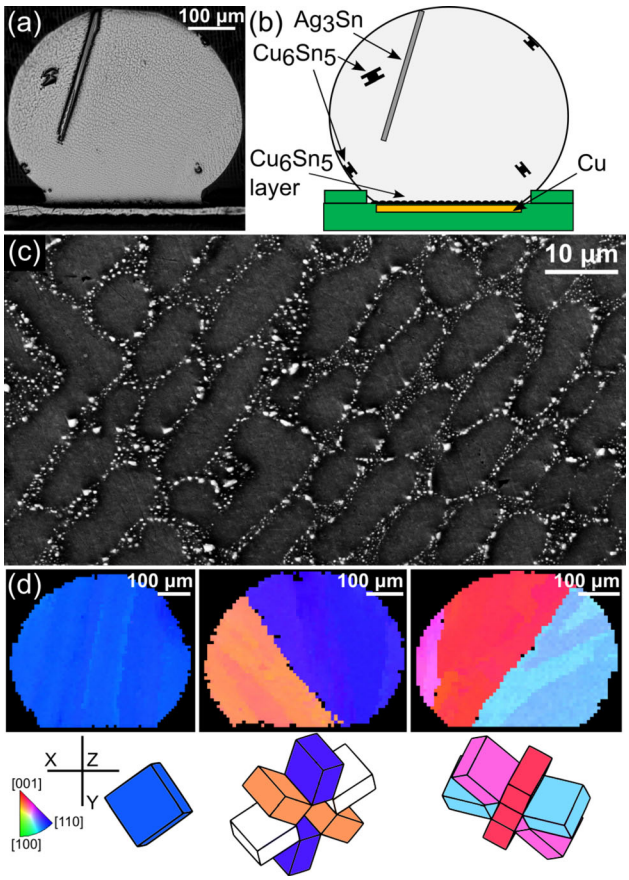

Fig. 2—Typical SAC305 solder joint microstructures from the present work. (*a*) Optical micrograph of a solder joint. (*b*) Schematic of the solder joint in (a) with the large Ag_3Sn and Cu_6Sn_5 that formed before β-Sn nucleation labeled as well as the Cu_6Sn_5 reaction layer on the Cu substrate. (*c*) Higher magnification SEM–BSE image within a joint showing β-Sn dendrites and β-Sn + Ag_3Sn + Cu_6Sn_5 eutectic. (*d*) EBSD orientation maps for single-grain (left) and cyclic-twinned (middle and right) solder joints. The maps from left to right are colored by IPF-Y, IPF-Y, and IPF-X. The unit cell wireframes of the β-Sn orientations are plotted below. The white orientation was not measured in this cross section and was calculated (Color figure online).

III. RESULTS AND DISCUSSION

A. *Overview of Obtained Microstructures*

Both single-grain and cyclic-twinned beachball microstructures solidified in the SAC305/Cu solder joints from both reflow soldering and DSC experiments. Figure 2(a) shows a typical optical micrograph taken from one of the solder joints, and Figure 2(b) shows a schematic labeling the large Ag_3Sn and Cu_6Sn_5 intermetallic compounds (IMCs) that formed prior to β-Sn nucleation, and the Cu_6Sn_5 reaction layer on the Cu substrate. The β-Sn dendrites are too fine to be observed at the magnification in Figure 2(a) but can be seen at higher magnification in Figure 2(c) with eutectic between the dendrite arms. Figure 2(d) gives examples of EBSD orientation maps [inverse pole figure (IPF) maps] of the β-Sn phase for single-grain and two multi-grain cyclic-twinned joints. It is likely that the middle joint in Figure 2(d) contains three orientations in 3D and the third, unmeasured orientation was calculated and plotted as a white wireframe. In all joints studied in this work, the dendrite growth pattern was consistent with nucleation having occurred on/near the Cu_6Sn_5 reaction layer at the bottom of the joint followed by upward dendrite growth consistent with past work on SAC305/Cu half-joints.[2]

To study whether the β-Sn nucleation orientation plays a role in cyclic twinning, EBSD maps of 29 SAC305 solder joints from DSC experiments with β-Sn nucleation undercoolings in the narrow range of 25 K to 30 K (*e.g.*, Figure 3(a)) were used to remove the effects of melt undercooling on dendrite growth.[26] For each joint, the minimum angle between the β-Sn $\langle 001 \rangle$ axis and the substrate plane normal (*i.e.*, the *Y* axis in the schematic in Figure 3(b)) was calculated from the Euler angles measured with EBSD and defined as θ. The results are plotted in Figure 3(b) with β-Sn grain morphology as the vertical axis. For each cyclic-twinned joint, only the β-Sn grain that has the minimum θ is plotted. Figure 3(b) shows that the θ of single-grain and cyclic-twinned solder joints both took almost the whole range of possible values, indicating that the β-Sn nucleation orientation does not influence whether or not cyclic twinning occurs. This is consistent with the interpretation of Lehman *et al.*[1] that cyclic twinning is determined at the nucleation stage rather than during growth. Notably, in Figure 3(b), the θ of single-grain joints was as low as 9.5 deg where all four preferred $\langle 110 \rangle$ growth directions are almost parallel to the substrate and badly oriented for upward $\langle 110 \rangle$ growth.

B. *Dendrite Growth in Single-Grain Joints*

When cross sections contained long straight dendrite trunks, they were usually approximately along $\langle 110 \rangle$. For example, Figures 4(a) and (b) are optical micrographs of a single-grain joint sectioned through an array of dendrite trunks. The arrow in Figure 4(b) indicates

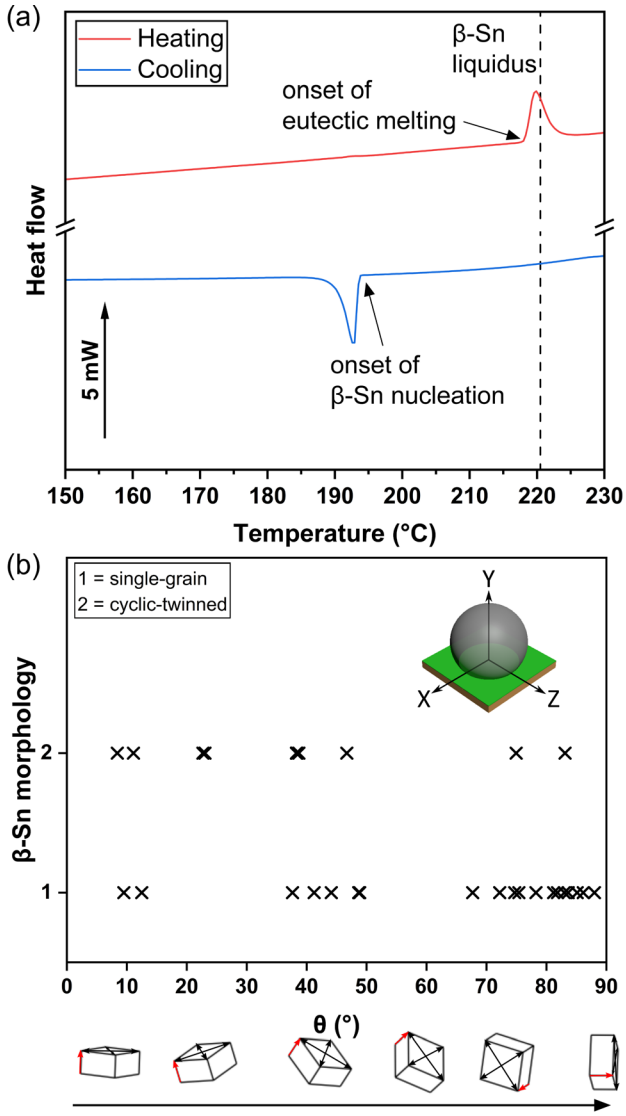

Fig. 3—(*a*) Thermal profile of melting and re-solidifying SAC305 in DSC. β-Sn nucleation undercooling = β-Sn liquidus temperature − β-Sn nucleation onset temperature. (*b*) Scatter plot of β-Sn grain morphology *vs* θ (the angle between ⟨001⟩ and the substrate plane normal, *Y*) for 29 solder joints with nucleation undercoolings in the narrow range of 25 K to 30 K. Below the plot are β-Sn unit cell wireframes with different θ angles, where the ⟨110⟩ directions are shown with black arrows and the ⟨001⟩ direction as a red arrow (Color figure online).

the direction of long continuous trunks. Although the actual dendrite growth direction is in 3D, a long trunk in the cross section indicates that the actual growth direction is close to its projection onto the sectioning plane. Figure 4(c) plots the ⟨110⟩ pole figure of the joint together with this dendrite growth vector, showing that the dendrite growth direction is approximately ⟨110⟩.

A similar procedure was performed on the long straight dendrite trunks from 43 SAC305/Cu joints (both single-grain and cyclic-twinned joints) and the Euler angles of their corresponding β-Sn grains were collected. With the dendrite growth vectors and the Euler angles of the grains, the lattice direction of dendrite growth was calculated for each dendrite trunk and plotted in a β-Sn inverse pole figure convolution plot in Figure 4(d). The dendrite growth directions are all close to ⟨110⟩, but the data are spread out and also encompass the ⟨221⟩ direction. The spread of growth directions in Figure 4(d) is affected by the use of 2D projected vectors rather than the actual 3D growth vectors and, therefore, only a broad conclusion can be drawn from Figure 4(d) that the long straight dendrite trunks grow approximately along ⟨110⟩.

In Figure 3(b), single-grain joints with small θ were relatively rare. To understand this, it is necessary to compare the measured angles with the angles expected of randomly oriented grains. EBSD data of 212 single-grain joints were collected, and their θ angles were calculated. The distribution of θ is plotted in Figure 5 and compared with the frequency curve of the calculated θ distribution from 10,000,000 randomly generated β-Sn orientations in MTEX.[27] The distribution of experimental data is close to what would be expected for randomly orientated β-Sn, suggesting that the orientation of β-Sn at the point of nucleation in a single-grain joint is near-random.

Despite the near-random β-Sn orientations, θ of the β-Sn grains is not evenly distributed: The ⟨001⟩ direction of a single-grain solder joint is more likely to be far away from the substrate plane normal (*i.e.*, the *Y* direction in Figure 5) and this is why there are few joints in Figures 3(b) and 5 with small θ. The shape of this random grain orientation distribution has been highlighted by other authors[13,14,28] who used it to argue that most single-grain solder joints would have relatively large coefficient of thermal expansion (CTE) mismatch between the solder and the substrate which is undesirable for reliability in thermal cycling. In the context of dendrite growth in BGA joints, this random grain orientation distribution in Figure 5 means that it is relatively rare for single-grain joints to have the worst orientation for upward ⟨110⟩ growth but, since there are many joints interconnecting an electronic package [*e.g.*, 84 in the 84CTBGA in Figures 1(a) and (b) and often more in other package types], it is common for some joints to be badly orientated for upward ⟨110⟩ growth.

To explore how the growth pattern of β-Sn dendrites in single-grain solder joints depends on the β-Sn orientation, optical micrographs of joints with different β-Sn orientations were collected and compared with orientation measurements from EBSD, as overviewed in Figure 6. Figure 6(a) exhibits the microstructure of a joint that is fairly well-oriented for upward ⟨110⟩ growth and has its β-Sn ⟨001⟩ almost normal to the cross section. Such a β-Sn orientation and cross section are ideal to study near-⟨110⟩ β-Sn dendrite growth. Repeated β-Sn dendrite branching of ~ 90 deg along [110] and [1$\bar{1}$0] can be clearly observed by comparing the micrograph and unit cell wireframes, resulting in zig-zag growth of the dendrites which formed a "web" and filled the space in the cross section.

Figure 6(b) shows the microstructure of another solder joint which has similar θ but has the β-Sn ⟨001⟩ lying almost in the sectioning plane. This cross section is ideal for the observation of dendrite growth out of the

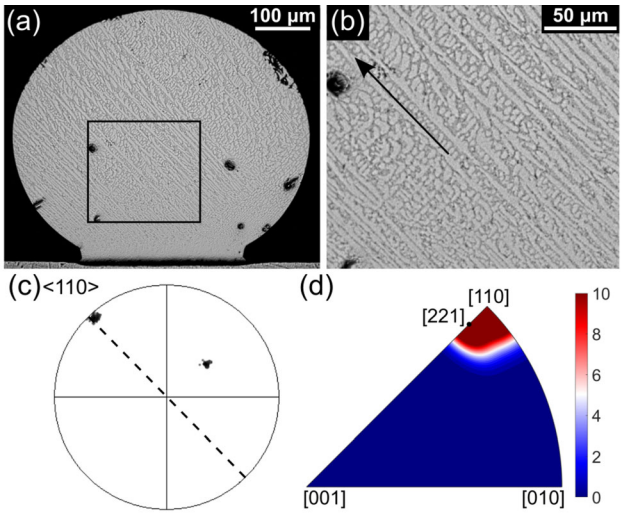

Fig. 4—Growth direction of long straight β-Sn dendrite trunks. (*a*) Optical micrograph of a whole joint. (*b*) Higher magnification micrograph of the boxed area in (a). The dendrite growth direction is marked with an arrow. (*c*) β-Sn ⟨100⟩ pole figure drawn with the dendrite growth direction (the dashed line) from (b). (*d*) Inverse pole figure convolution plot of the main β-Sn dendrite growth directions from 43 solder joints.

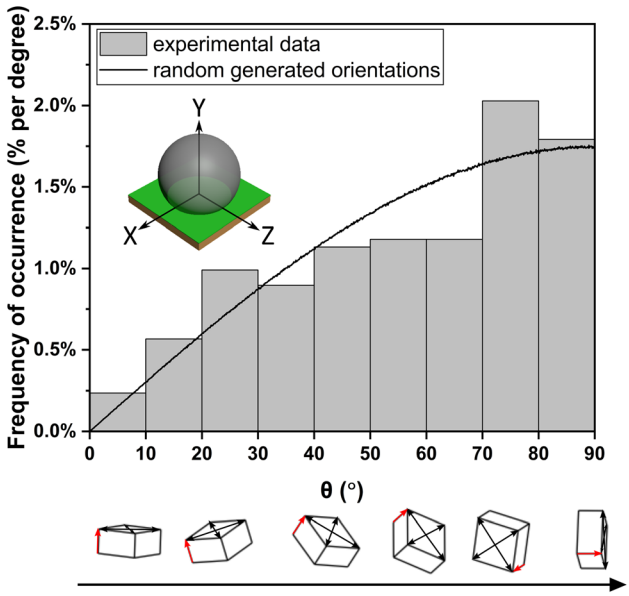

Fig. 5—Distribution of θ (the angle between ⟨001⟩ and the substrate plane normal, *Y*) for both experimental data of single-grain solder joints and randomly generated orientations.

{001} plane. It is clear from the micrograph that out-of-plane dendrite tip splitting and branching occurred followed by growth with an out-of-{001}-plane component. Comparing the dendrite tip growth directions from the zoomed-in micrograph with the β-Sn orientation in Figure 6(b), the ⟨11*W*⟩ growth directions that deviated the most were close to ⟨111⟩. The growth of these tips helped β-Sn dendrites to fan out outside the {001} that confines the ⟨110⟩ and fill the solder volume. By combining Figures 6(a) and (b), the growth pattern

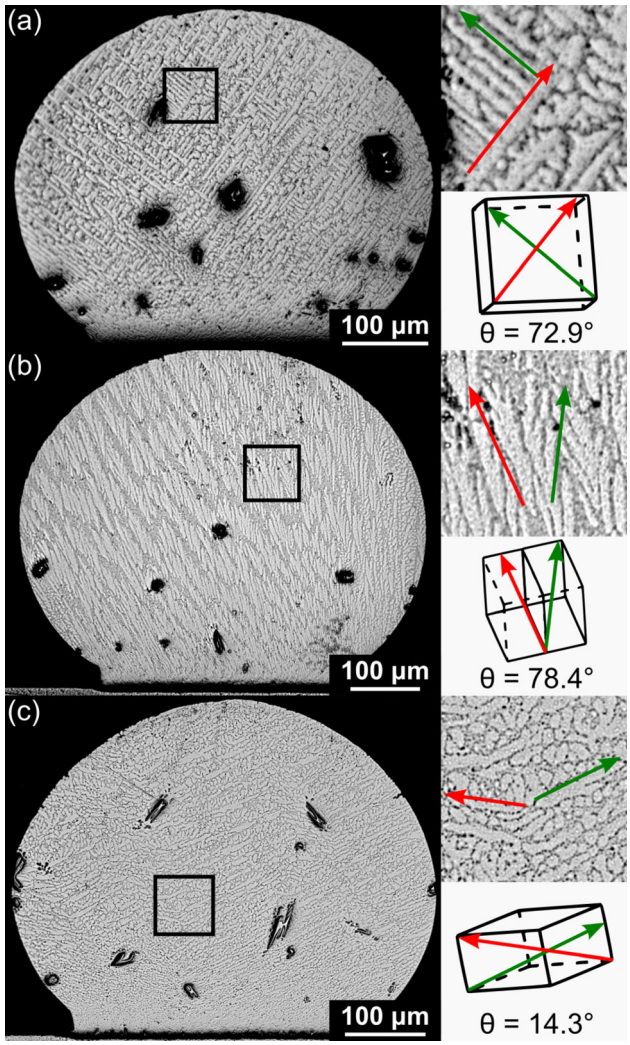

Fig. 6—Optical micrographs of single-grain solder joints with (*a*) β-Sn ⟨001⟩ almost normal to the sectioning plane with large θ (the angle between ⟨001⟩ and the substrate plane normal), (*b*) β-Sn ⟨001⟩ almost in the sectioning plane with large θ, and (*c*) β-Sn ⟨001⟩ almost in the sectioning plane with small θ. The β-Sn unit cell wireframe orientations were plotted from Euler angles measured by EBSD (Color figure online).

of β-Sn dendrites in a single-grain solder joint with reasonably well-oriented β-Sn (when θ is not small) can be summarized as follows: in {001}, the dendrites grow along ⟨110⟩ and fill the plane with repeated 90 deg ⟨110⟩ branching. In the meantime, dendrite tip splitting happens outside {001} followed by further growth along ⟨11*W*⟩, usually with a range of directions spanning $0 < W \leq 1$, which enables the dendrite to fill the spheroidal solder volume.

Next, we consider how β-Sn dendrites grow to fill the volume when the β-Sn is badly oriented for upward growth. A single-grain solder joint with a small θ of 14.3 deg is presented in Figure 6(c). Two main dendrite growth directions can be seen in the micrograph (marked as red and green arrows in the zoomed-in micrograph), both of which have different ⟨11*W*⟩ directions (*e.g.*, $[11W_1]$ and $[\bar{1}1W_2]$). Zig-zag dendrite branching with these two growth directions can be

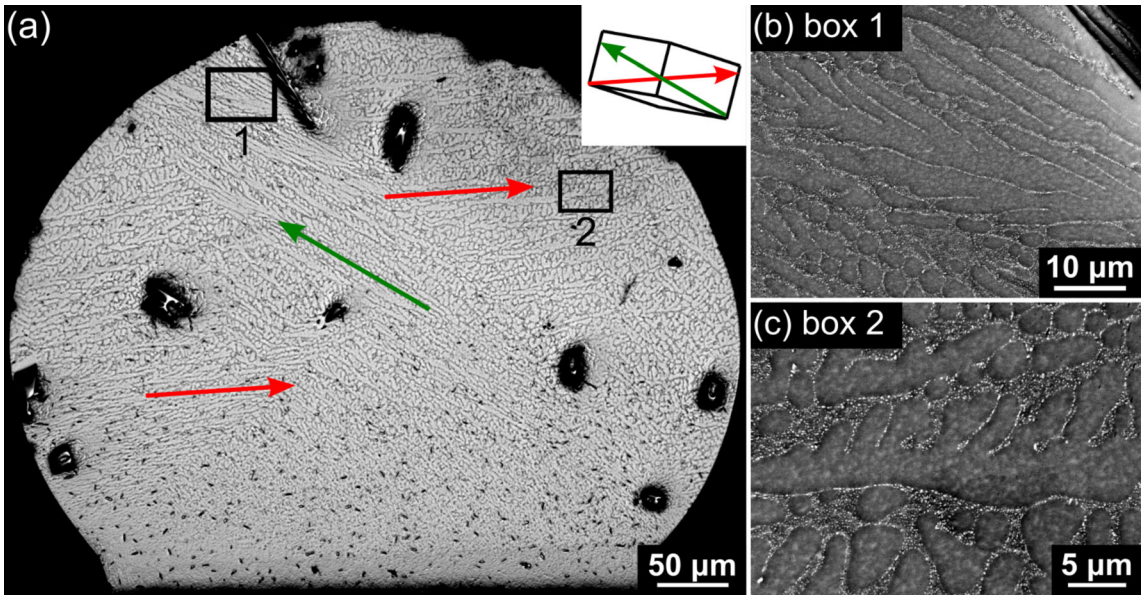

Fig. 7—Another single-grain solder joint with β-Sn $\langle 001 \rangle$ almost in the sectioning plane and small θ (the angle between $\langle 001 \rangle$ and the substrate plane normal). (*a*) Optical micrograph along with unit cell wireframe of the β-Sn orientation. The two $\langle 11W \rangle$ growth directions are marked with red and green arrows. (*b*) Backscattered SEM image from box 1 in (a) that shows dendrite tip splitting. (*c*) Backscattered SEM image from box 2 in (a) that shows some near-$\langle 001 \rangle$ secondary dendrite arms (Color figure online).

observed in the microstructure which enables growth out of the {001} plane to fill the 3D volume. Figure 7 shows more detail of the microstructure of another single-grain joint with small θ. Zig-zag dendrite branching with two $\langle 11W \rangle$ directions is observed [the red and green arrows in Figure 7(a)]. Here, the zig-zag angle is as high as 146.1 deg because the two $\langle 11W \rangle$ directions are only $\pm$ 16.1 to 17.8 deg outside of the {001}. This is a consequence of the low symmetry of tetragonal β-Sn which causes all four preferred $\langle 110 \rangle$ to be very badly oriented for upward growth and less preferred $\langle 11W \rangle$ become the main dendrite trunks but they still have a very high zig-zag angle since these $\langle 11W \rangle$ are only ~ 17 deg outside of the {001}. Besides the zig-zag branching of the main dendrite trunks, dendrite tip splitting (Figure 7(b)) was also found in these badly oriented single-grain joints, as well as the development of secondary dendrite arms with directions close to $\langle 001 \rangle$ (Figure 7(c)). Both of these mechanisms enable further β-Sn dendrite growth out of {001}.

Comparing dendrite growth in BGA joints with fairly well-oriented β-Sn in Figures 6(a) and (b) versus badly oriented β-Sn in Figures 6(c) and 7, we see that different types of zig-zag dendrite growth occurred to enable the dendrites to fill the spheroidal BGA volume. (i) when the θ angle between the $\langle 001 \rangle$ and Y axis was large (Figures 6(a) and (b)), the main dendrite trunks grew along $\langle 110 \rangle$ by a combination of zig-zag growth by repeated 90 deg branching along $\langle 110 \rangle$ (e.g., [110] and $[1\bar{1}0]$) and some out-of-plane dendrite tip splitting, branching and growth along $\langle 11W \rangle$. (ii) When the θ angle was small (Figures 6(c) and 7), zig-zag growth changed such that the main trunks now grew along $\langle 11W \rangle$ and the zig-zag growth was enabled by the W-component of growth. In the most badly oriented dendrites, this second type of zig-zag growth involved a high branching angle, typically > 140 deg.

In many situations in solidification and casting, there are numerous nucleation events followed by competitive growth such that those grains best oriented for growth are selected. However, with Sn–Ag–Cu BGA solder joints, there is only a single nucleation event with a random crystallographic orientation and, therefore, dendrites commonly grow with unfavorable orientations, resulting in the different types of zig-zag growth and branching presented above. We note that the β-Sn dendrite growth behavior reported here for Sn–3Ag–0.5Cu/Cu joints does not occur for all Pb-free solder compositions and is in stark contrast to Sn–0.7Cu/Cu joints. There, in BGA joints, numerous β-Sn nucleation events usually occur on/near both Cu_6Sn_5 reaction layers, enabling competitive growth followed by the columnar $\langle 110 \rangle$ growth of the selected grains which results in a strong $\langle 110 \rangle$ growth texture.[2]

C. *Dendrite Growth in Cyclic-Twinned Solder Joints*

EBSD data of 96 cyclic-twinned solder joints were collected, and the angles between their $\langle 100 \rangle$ common twinning axis and Y (the substrate normal) were calculated from the measured Euler angles. The data are compared with the frequency curve of random orientations in Figure 8(a). In addition, for each of these solder joints, one of the β-Sn orientations was randomly selected and its θ (the angle between $\langle 001 \rangle$ axis and Y) was calculated. Figure 8(b) compares the θ distribution of these joints with the frequency curve calculated from randomly generated orientations. Figures 8(a) and (b) indicate that the orientations of both the cyclic twinning axis and the individual β-Sn grains in cyclic-twinned

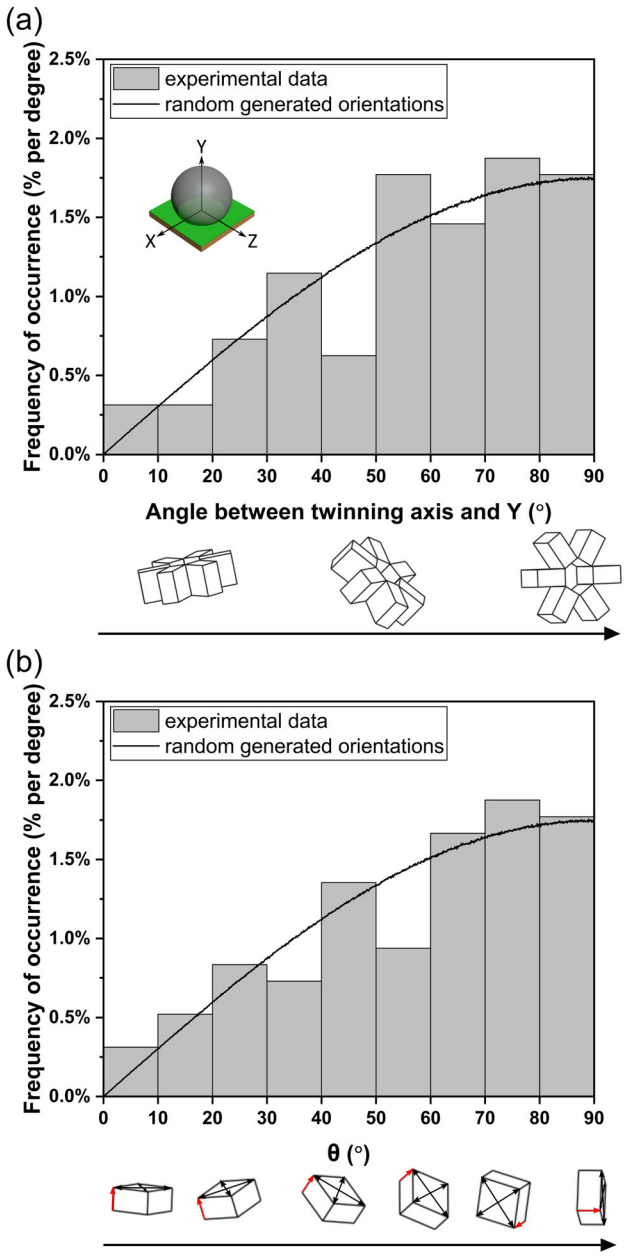

Fig. 8—Orientation distribution of 96 cyclic-twinned solder joints. (*a*) Distribution of the angles between the ⟨100⟩ twinning axis and *Y* for experimental data of cyclic-twinned solder joints (the bar chart) and the angle between randomly generated directions and *Y* (the curve). (*b*) Distribution of θ (the angle between ⟨001⟩ and the substrate plane normal, *Y*) for one randomly selected orientation in each cyclic-twinned solder joint (the bar chart) and the calculated curve from randomly generated orientations.

joints are near-random. This is similar to the orientations in single-grain joints in Figure 5.

Figure 9(a) shows the microstructure of a typical cyclic-twinned "beachball" joint using a polarized optical micrograph. The orientations of the three β-Sn grains were measured with EBSD and are plotted in Figure 9(a) as unit cell wireframes. The ⟨110⟩ main growth directions of the grains are marked in Figure 9(a) as well as the substrate normal *Y* and the lateral axis *X*. The minimum angle between the ⟨110⟩

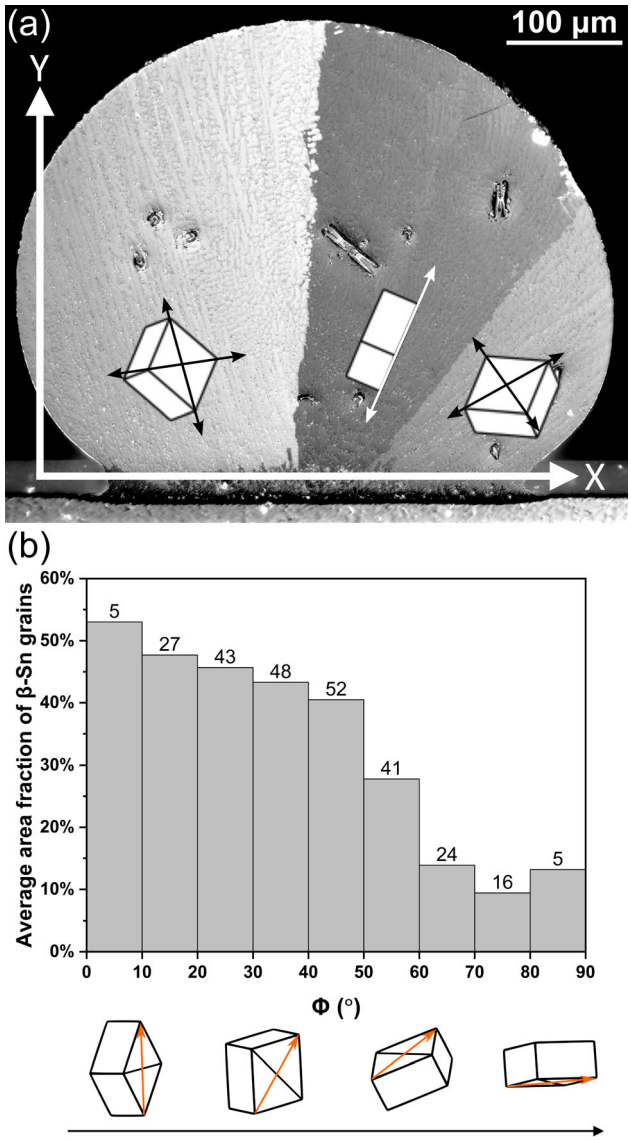

Fig. 9—The relationship between β-Sn grain volume fraction and orientation in beachball joints. (*a*) Polarized optical micrograph of a typical cyclic-twinned solder joint with unit cell wireframes of the β-Sn orientations. (*b*) Bar chart of the average area fraction of β-Sn grains *vs* φ (the minimum angle between ⟨110⟩ and *Y*). The numbers above each bar are the number of grains measured for each bar.

directions and *Y* for each grain was defined as φ. φ of 230 β-Sn grains from 84 cyclic-twinned joints was calculated. The area fraction of these β-Sn grains in the corresponding joints was measured from polarized optical micrographs and plotted against φ as a bar chart in Figure 9(b). Note that the bars in Figure 9(b) show the mean area fraction from grains in multiple joints to minimize cross-sectioning effects. At least 16 grains make up each bar except for the outermost bars. It is clear that when the φ angle of a β-Sn grain is small, this grain is more likely to occupy a larger area fraction in the solder joint cross section. This result indicates that there is competitive dendrite growth among the three cyclic-twinned orientations, where grains having at least one ⟨110⟩ direction well-oriented for growth (*i.e.*, with a

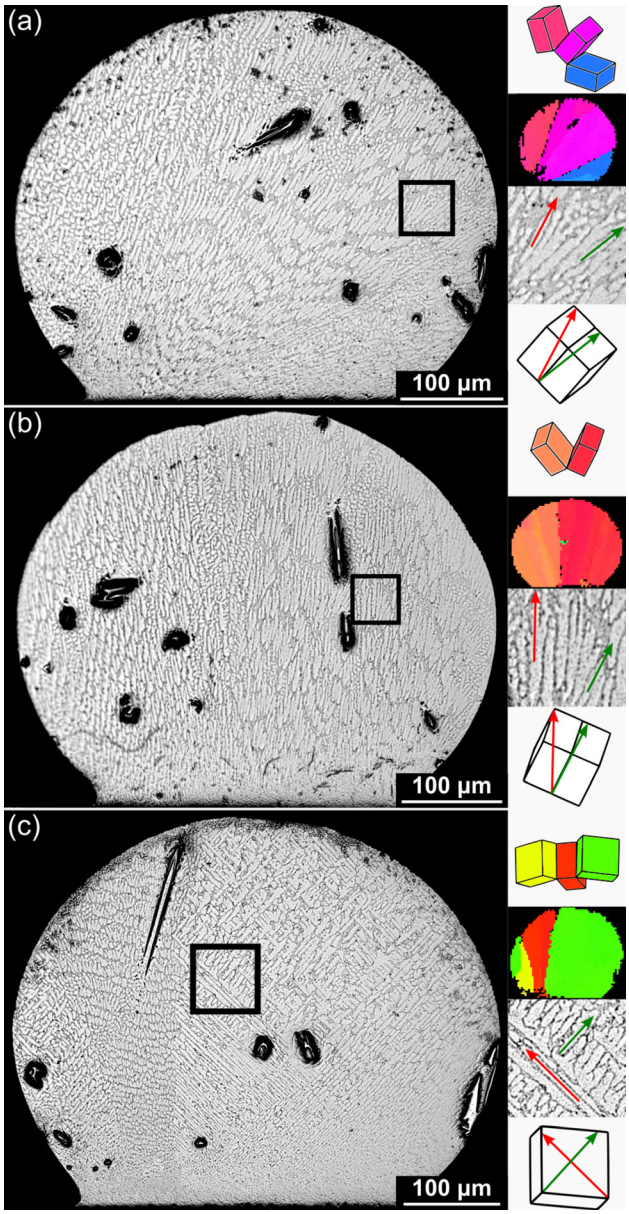

Fig. 10—β-Sn dendrite growth patterns in three cyclic-twinned joints. (*a*) and (*b*) show out-of-{001}-plane dendrite growth and (*c*) highlights in-{001}-plane ⟨110⟩ dendrite growth. For each joint, the optical micrograph is on the left, and the panels on the right are (from top to bottom): unit cell wireframes, IPF orientation maps, zoomed-in optical micrograph of the boxed region, and unit cell wireframe of the boxed region (Color figure online).

small φ angle) outcompete less well-oriented grains and grow to fill a larger volume fraction of the joint.

The general features of dendrite growth in cyclic-twinned joints were similar to single-grain joints. To demonstrate the out-of-{001}-plane dendrite growth, two joints with their ⟨001⟩ lying almost in the sectioning plane are overviewed in Figures 10(a) and (b). In these examples, many instances can be observed of dendrite tip splitting followed by growth of the split tips along $\langle 11W \rangle$ growth directions. It is observed that the split tips that deviated the most from ⟨110⟩ in both joints have growth directions close to ⟨111⟩. In comparison, Figure 10(c) shows the β-Sn dendrite growth and orientations of a cyclic-twinned joint with the ⟨001⟩ axis of one of its β-Sn grains (the green grain) almost perpendicular to the cross section. The zig-zag growth by repeated 90 deg ⟨110⟩ branching can be observed in this grain from the zoomed-in micrograph, which is similar to what was observed from the single-grain joints (*e.g.*, Figure 6(a)).

Figure 11 overviews how these crystallographic dendrite growth features lead to the beachball morphology in cyclic-twinned joints. Figure 11(a) shows an IPF map of a cyclic-twinned solder joint with ⟨001⟩ of one of its β-Sn grains almost parallel to the cross section. Figure 11(b) shows a schematic of the grain structure with the unit cell wireframes plotted along with a linear approximation of the three grain boundaries. Clear dendrite tip splitting can be seen in grain B in both the optical micrograph in Figure 11(c) and the SEM image in Figure 11(d), which enables the dendrite to fan out in $\langle 11W \rangle$ directions with varying values of W.

Figures 11(e) and (f) show polarized optical micrographs of the microstructure spanning the two grain boundaries in this cross section. The dendrite growth directions that are close to the grain boundaries are highlighted in the micrographs with arrows. Note in Figures 11(e) and (f) that, when the dendrite trunks from the two neighboring grains are close to the grain boundary between them, they tend to have growth directions that are nearly parallel with each other, and also nearly parallel with the grain boundary. These dendrite growth directions are plotted on the unit cell wireframes in Figure 11(b) which shows these near-grain-boundary β-Sn dendrite trunks did not tilt beyond the ⟨111⟩ directions. It is shown next that the grain boundary planes are approximately the $\{10\bar{1}\}$ that contain these ⟨111⟩ trunk directions in each of the two neighboring grains.

The β-Sn ⟨111⟩ and $\{10\bar{1}\}$ pole figures of the solder joint in Figures 11(a) through (f) are shown in Figures 11(g) and (h). Because of the crystallography of β-Sn cyclic twinning,[1] some of the ⟨111⟩ directions and $\{10\bar{1}\}$ planes are shared by pairs of grains in the pole figures. For example, the cyan and red orientations share two ⟨111⟩ spots and one $\{10\bar{1}\}$ spot, as highlighted with the yellow circles. The dashed blue, yellow, and orange lines on the $\{10\bar{1}\}$ pole figure in Figure 11(h) are bisectors containing the projected plane normals of the grain boundaries in the cross section in Figures 11(b), (e), and (f). All the three dashed lines pass through the $\{10\bar{1}\}$ spots that are shared by the two grains on either side of the relevant grain boundary, indicating that $\{10\bar{1}\}$ is the grain boundary plane for these boundaries. To examine the generality of this, 34 cyclic-twinned joints with almost-straight long grain boundaries were studied. For each grain boundary, the lattice directions lying in the grain boundary plane were calculated using the grain orientations on either side of the boundary and plotted in the β-Sn inverse pole figure in Figure 11(i) along with the trace of $\{10\bar{1}\}$. It is clear from Figure 11(i) that all the long straight grain boundary lines have lattice directions that nearly lie in the $\{10\bar{1}\}$,

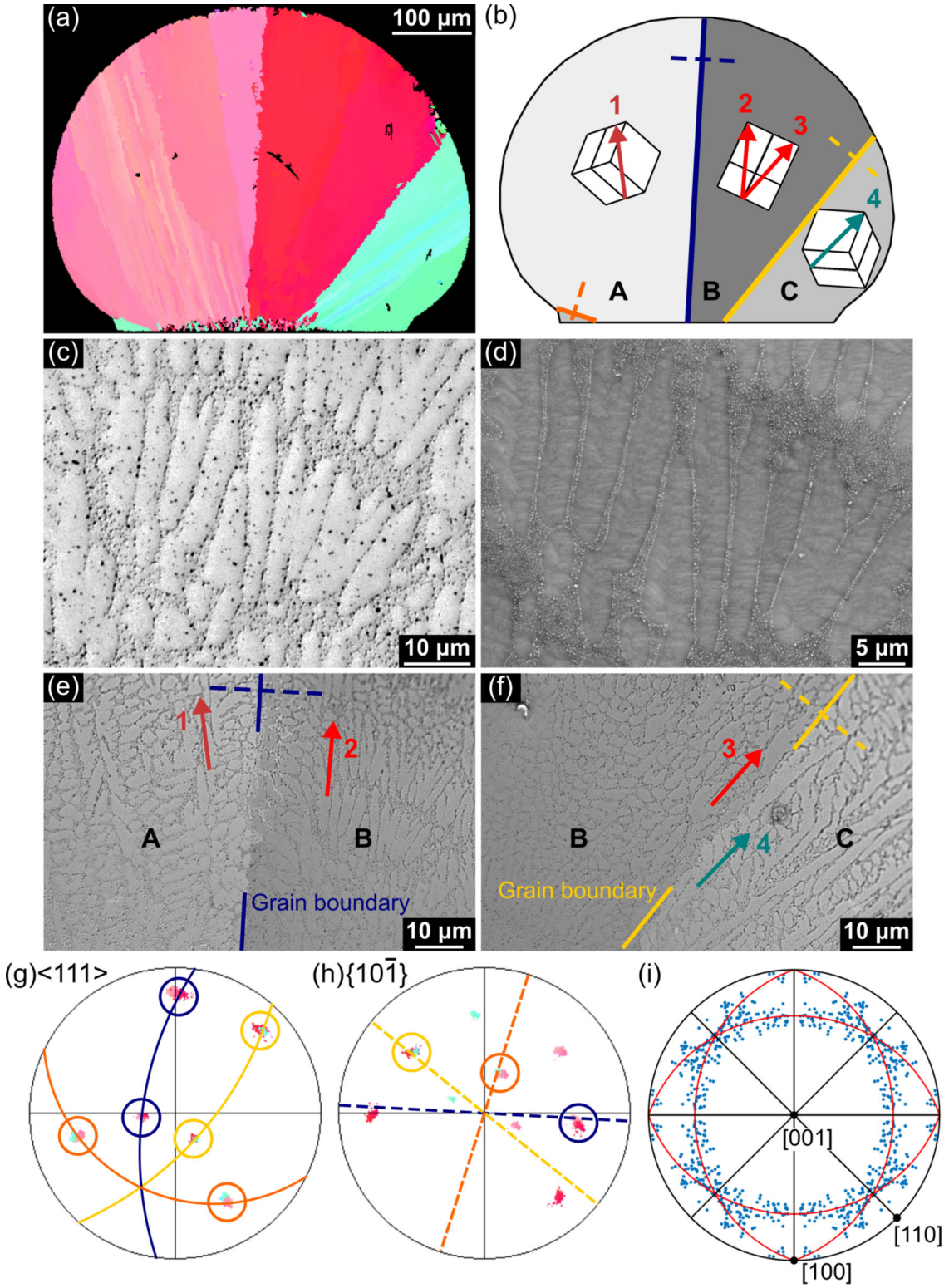

Fig. 11—The formation of beachball boundaries by β-Sn dendrite tip splitting and $\langle 11W \rangle$ trunk growth. (*a*) through (*h*) are all associated with the same solder joint. (a) EBSD orientation map of a beachball SAC305 solder joint. (b) Schematic defining grain boundaries (blue, yellow, and orange) with β-Sn unit cell wireframes from EBSD. (c), (d) Dendrite tip splitting in the red grain in (a), enabling the fanning out of trunks along $\langle 11W \rangle$. (c) is an optical micrograph, (d) is a backscattered SEM image. (e), (f) Polarized optical micrographs of the microstructure near the two grain boundaries. The β-Sn dendrite growth directions near the grain boundaries are highlighted with arrows and superimposed on unit cells in (b). The maximum $\langle 11W \rangle$ reached is approximately $\langle 111 \rangle$. (g) $\langle 111 \rangle$ pole figure for β-Sn. Pairs of $\langle 111 \rangle$ that are parallel in neighboring grains are highlighted with circles. The solid lines are the trace of the $\{10\bar{1}\}$ showing that the two pairs of $\langle 111 \rangle$ shared between neighboring grains both lie in the shared $\{10\bar{1}\}$. (h) $\{10\bar{1}\}$ pole figure for β-Sn. The dashed lines are normals to the grain boundaries drawn in (b) and intersect the $\{10\bar{1}\}$ planes shared by each pair of neighboring β-Sn grains (circled). (*i*) Measured lattice directions lying in beachball grain boundaries from 34 joints plotted on a β-Sn inverse pole figure. The red lines are the traces of $\{10\bar{1}\}$, confirming that beachball boundaries are approximately $\{10\bar{1}\}$ (Color figure online).

confirming that the common $\{10\bar{1}\}$ plane shared by two neighboring β-Sn grains is usually the grain boundary plane between them. Note, however, that this is only true at the macro-scale and beachball boundaries such as those in Figures 11(a), (e), (f) are wavy at the scale of the dendrites. This incoherent twin boundary forms when dendrites related by a near-twin relationship impinge on one another during growth, which is only possible because of the fanning out of $\langle 11W \rangle$ dendrite trunks which causes impingement when parallel neighboring $\langle 111 \rangle$ trunks meet at their shared $\{10\bar{1}\}$. This is illustrated in Figures 12(a) through (c). When the trunks on either side of the $\{10\bar{1}\}$ boundary are both growing along $\langle 111 \rangle$, they grow at the same velocity and the wavy $\{10\bar{1}\}$ boundary is maintained all the way to the edge of the solder ball (*e.g.*, Figure 11(a)). The observed beachball microstructures also indicate that dendrite trunks with growth directions closer to $\langle 110 \rangle$ grow faster, and there is a growth competition between the trunks of two neighboring grains such that trunks growing along $\langle 11W \rangle$ with $W > 1$ are outcompeted (overgrown) by the dendrites of neighboring grains with trunks growing along $\langle 111 \rangle$ directions.

Note that cyclic-twinned dendrite growth did not result in the very high zig-zag angle (>140 deg) observed in the worst-oriented single-grain joints (Figure 7) because dendrites that are badly oriented for growth in beachballs are outcompeted by a neighboring dendrite that is better oriented for growth. For example, in Figure 10(a), the blue grain is badly oriented for upward $\langle 110 \rangle$ dendrite growth and is outcompeted by its neighboring magenta dendrite in that direction. The orientations of the magenta and blue grains result in a $\{10\bar{1}\}$ boundary with a small angle to the substrate, which results in the small volume fraction of the blue grain. This is the origin of the orientation effect on the area fraction of β-Sn grains shown in Figure 9(b). At the same time, the blue dendrite in Figure 10(a) is better oriented than the magenta dendrite to grow into the very bottom-right of the ball and has growth advantages in this small region. Indeed, in a BGA ball, three cyclic-twinned grains growing from a point on the Cu_6Sn_5 layer have a growth advantage over a single-grain joint because dendrites of all three orientations can grow to fill all parts of the volume without the need for unfavorable growth involving high zig-zag angles (*e.g.*, > 140 deg). This is why all three orientations survive during competitive growth in a BGA ball giving beachball microstructures. In summary, while the crystallographic geometry of the cyclic twin formed at the nucleation stage determines the orientation relationship between the three grains as shown by Lehman *et al.*,[1] it is the competitive growth between the dendrites that produces the $\{10\bar{1}\}$ beachball boundaries and, therefore, the beachball microstructure.

Finally, it is instructive to compare cyclic-twinned dendrite growth in β-Sn with prior work on twinned dendrite growth in other nonfaceted metal systems. In FCC metals including aluminum and gold alloys, Kurtuldu *et al.*[29,30] and others[31–33] have identified aggregates of multiple grains interrelated by a

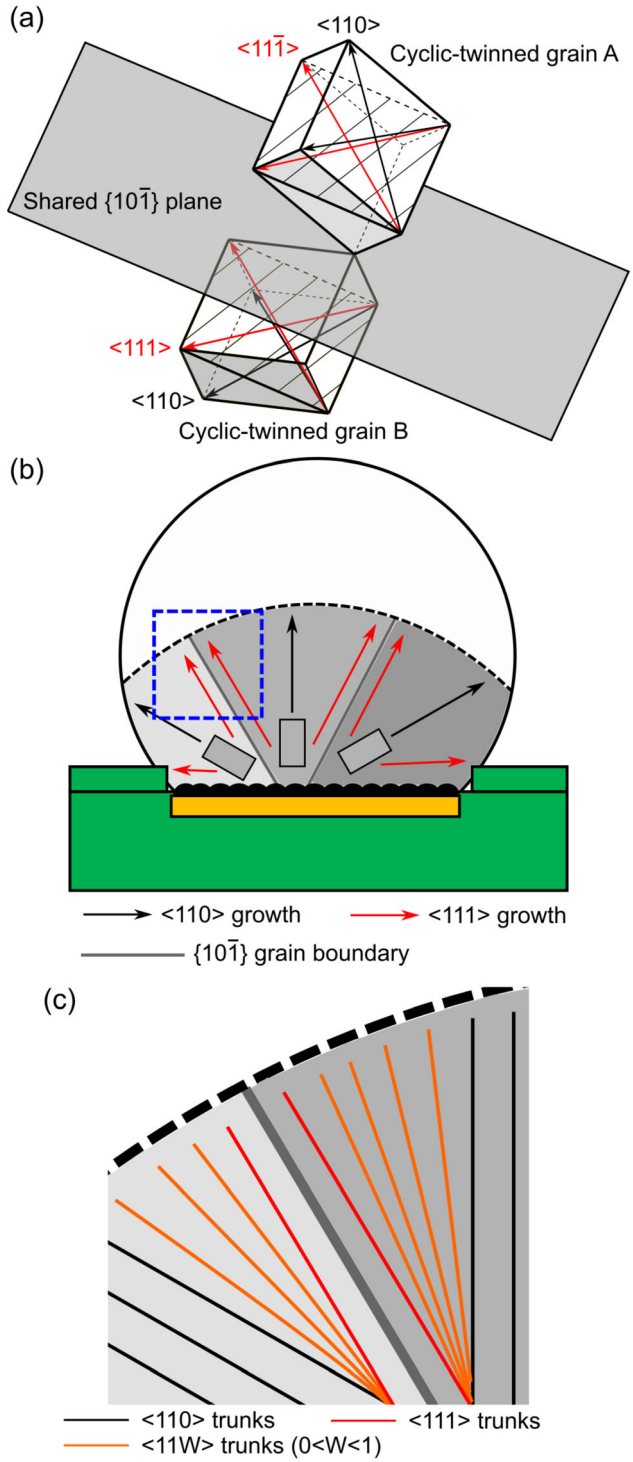

Fig. 12—Formation of the beachball microstructure from dendrite growth of three cyclic-twinned orientations growing from a point on/near the Cu_6Sn_5 layer. (*a*) 3D illustration showing that two $\langle 111 \rangle$ trunk directions of each neighboring grain all lie in a shared $\{10\bar{1}\}$ plane. (*b*) Schematic of cyclic-twinned β-Sn dendrite growth directions leading to the formation of $\{10\bar{1}\}$ boundaries and the beachball microstructure. The $\langle 010 \rangle$ twin axis is normal to the cross section. (*c*) Schematic of the boxed region in (b) highlighting how the fanning out of dendrite trunks causes neighboring $\langle 111 \rangle$ to meet at their shared $\{10\bar{1}\}$. N.B. (c) is highly simplified, showing trunks but not secondary arms, schematising tip splitting and omitting other dendrite growth mechanisms.

near-{111} twin relationship which they attributed to icosahedral short-range order (ISRO) in the liquid and/or the formation of an icosahedral precursor phase on which the FCC phase solidifies into a multiply twinned aggregate. While the symmetry of cyclic twinning in β-Sn is different, there are similarities in that the three β-Sn orientations seem to form at the nucleation stage which has been discussed by Lehman *et al.*[1] in terms of a nucleus with hexagonal symmetry.

Twinned dendrite growth in aluminum alloys has been studied in detail.[34–38] There, twinned α-Al dendrites grow along $\langle 110 \rangle$ instead of the more common $\langle 100 \rangle$ and have a coherent $\Sigma 3$ {111} twin plane running down the center of their trunk. This is different to the case of cyclic-twinned β-Sn where each dendrite is a single crystal and is in a near-twin relationship with the neighboring single-crystal dendrite. However, there is also a key similarity: Henry *et al.*[39] showed that, when twinned α-Al dendrites grow as a parallel array of twinned trunks, the secondary arms of neighboring trunks impinge to form wavy incoherent twin boundaries. This is similar to the wavy $\{10\bar{1}\}$ near-twin boundaries created when neighboring β-Sn dendrites impinge to create the beachball microstructure (Figures 11 and 12), although the symmetry and details of branching are different.

IV. CONCLUSIONS

This work has revealed the following new insights into β-Sn dendrite growth in 500 μm diameter Sn–3Ag–0.5Cu ball grid array (BGA) solder joints where nucleation occurs in an undercooled liquid on/near the Cu_6Sn_5 layer followed by upward β-Sn dendrite growth.

(1) While $\langle 110 \rangle$ is the dominant dendrite growth direction, out-of-plane branching and growth with $\langle 11W \rangle$ directions are important for allowing dendrites to fan out into the spheroidal volume of BGA joints due to the low symmetry of β-Sn.
(2) A statistical comparison of measured and calculated grain orientations revealed that nucleation produces near-random β-Sn orientations in both single-grain and cyclic-twinned BGA joints. Due to the shape of the random distribution curve, there is a relatively low probability of joints having their {001} plane lying in the plane of the printed circuit board (PCB) which is the worst orientation for upward $\langle 110 \rangle$ growth. However, due to the large number of joints in an electronic package, random nucleation will produce some balls that are badly oriented for dendrite growth.
(3) The crystallographic orientation of β-Sn at the nucleation point plays a strong role in subsequent dendrite growth. This is a particularly strong effect in single-grain joints where the worst-oriented dendrites rely on trunk growth along $\langle 11W \rangle$ and large trunk branching angles of > 140 deg to achieve upward dendrite growth and fill the volume. In contrast, well-oriented dendrites can grow upward with the preferred $\langle 110 \rangle$ directions, although some out-of-plane branching is still required to fill the spheroidal volume.
(4) In cyclic-twinned joints, while the orientation relationship between the three β-Sn orientations is formed at/near the nucleation stage as shown by Lehman *et al.*,[1] it is the competitive growth between the dendrites that produces the $\{10\bar{1}\}$ beachball boundaries and, therefore, the beachball microstructure. A beachball microstructure is created when out-of-plane $\langle 11W \rangle$ branching and growth cause trunks of neighboring dendrites to impinge with their $\langle 111 \rangle$ trunks near-parallel. This causes the neighboring $\langle 111 \rangle$ trunks in two dendrites to grow in the same direction at the same velocity and form a long wavy $\{10\bar{1}\}$ boundary. Simple beachball microstructures form when $\{10\bar{1}\}$ boundaries develop in this way between all neighboring dendrites.

ACKNOWLEDGMENTS

The authors gratefully acknowledge the use of characterization facilities within the Harvey Flower Electron Microscopy Suite, Department of Materials, Imperial College London. This work was partially funded by the UK EPSRC Grant EP/R018863/1.

CONFLICT OF INTEREST

On behalf of all authors, the corresponding author states that there is no conflict of interest.

REFERENCES

1. L.P. Lehman, Y. Xing, T.R. Bieler, and E.J. Cotts: *Acta Mater.*, 2010, vol. 58, pp. 3546–56.
2. J.W. Xian, Z.L. Ma, S.A. Belyakov, M. Ollivier, and C.M. Gourlay: *Acta Mater.*, 2017, vol. 123, pp. 404–15.
3. L.P. Lehman, S.N. Athavale, T.Z. Fullem, A.C. Giamis, R.K. Kinyanjui, M. Lowenstein, K. Mather, R. Patel, D. Rae, J. Wang, Y. Xing, L. Zavalij, P. Borgesen, and E.J. Cotts: *J. Electron. Mater.*, 2004, vol. 33, pp. 1429–39.
4. M. Mueller, S. Wiese, and K.J. Wolter: *Proc. Electron. Components Technol. Conf.*, 2009, pp. 1027–36.
5. T.K. Lee, B. Zhou, L. Blair, K.C. Liu, and T.R. Bieler: *J. Electron. Mater.*, 2010, vol. 39, pp. 2588–97.
6. B. Arfaei, S. Mahin-Shirazi, S. Joshi, M. Anselm, P. Borgesen, E. Cotts, J. Wilcox, and R. Coyle: *Proc. Electron. Compon. Technol. Conf.*, 2013, pp. 976–85.
7. Z.L. Ma and C.M. Gourlay: *J. Alloys Compds*, 2017, vol. 706, pp. 596–608.
8. J. Han and F. Guo: *Microelectron. Reliab.*, 2019, vol. 98, pp. 1–9.
9. C. Fleshman and J.G. Duh: *J. Electron. Mater.*, 2020, vol. 49, pp. 196–201.
10. E. Ben Romdhane, P. Roumanille, A. Guédon-Gracia, S. Pin, P. Nguyen, and H. Frémont: *Microelectron. Reliab.*, 2021, vol. 126, p. 114288.
11. X.L. Ren, X.Y. Liu, S.Y. Shi, Y.P. Wang, and N. Zhao: *Mater. Charact.*, 2023, vol. 199, p. 112847.
12. B. Wang, X.J. Hu, W. Sun, J.L. Liao, H.L. Peng, N. Hou, B. Chen, and G. Zeng: *Mater. Charact.*, 2023, vol. 198, p. 112707.
13. T.R. Bieler, H. Jiang, L.P. Lehman, T. Kirkpatrick, E.J. Cotts, and B. Nandagopal: *IEEE Trans. Compon. Packag. Technol.*, 2008, vol. 31, pp. 370–81.
14. J.W. Xian, Y.L. Xu, S. Stoyanov, R.J. Coyle, F.P.E. Dunne, and C.M. Gourlay: *Nat. Commun.*, 2024, vol. 15, p. 4258.
15. F. Weinberg and B. Chalmers: *Can. J. Phys.*, 1952, vol. 30, pp. 488–502.
16. J.C. Warner and J.D. Verhoeven: *Metall. Trans.*, 1972, vol. 3, pp. 1001–02.
17. S. O'Hara: *Acta Metall.*, 1967, vol. 15, pp. 231–36.
18. S. O'Hara: *J. Cryst. Growth*, 1967, vol. 1, pp. 73–78.
19. G.L.F. Powell, G.A. Colligan, V.A. Surprenant, and A. Urquhart: *Metall. Trans. A*, 1977, vol. 8, pp. 971–73.
20. A.L. Genau and P.W. Voorhees: *Metall. Mater. Trans. A*, 2013, vol. 44A, pp. 406–18.
21. E. Çadirli and M. Gündüz: *J. Mater. Sci.*, 2000, vol. 35, pp. 3837–48.
22. H. Yasuda, I. Ohnaka, K. Kawasaki, A. Sugiyama, T. Ohmichi, J. Iwane, and K. Umetani: *J. Cryst. Growth*, 2004, vol. 262, pp. 645–52.
23. B.L. Silva, P.H. Mendes, A. Garcia, and J.E. Spinelli: *J. Electron. Mater.*, 2022, vol. 51, pp. 4640–48.
24. B.S. Sobral, P.S. Vieira, T.S. Lima, J.E. Spinelli, N. Cheung, A. Garcia, and B.L. Silva: *Adv. Eng. Mater.*, 2023, vol. 25, pp. 1–18.
25. R.B. de Sousa, J.L. Paixão, S.L. de Araújo Dantas, P.R.D. de Freitas, J.R.D. da Luz, J.E. Spinelli, and B.L. Silva: *J. Electron. Mater.*, 2023, vol. 52, pp. 7740–62.
26. B. Arfaei, N. Kim, and E.J. Cotts: *J. Electron. Mater.*, 2012, vol. 41, pp. 362–74.
27. R. Hielscher and H. Schaeben: *J. Appl. Crystallogr.*, 2008, vol. 41, pp. 1024–37.
28. A. Lovberg and P.E. Tegehall: *Proc. Electron. Compon. Technol. Conf.*, 2018, May 2018, pp. 882–89.
29. G. Kurtuldu, P. Jarry, and M. Rappaz: *Acta Mater.*, 2013, vol. 61, pp. 7098–7108.
30. G. Kurtuldu, A. Sicco, and M. Rappaz: *Acta Mater.*, 2014, vol. 70, pp. 240–48.
31. I. Cazic, J. Zollinger, S. Mathieu, M. El Kandaoui, P. Plapper, and B. Appolaire: *Scripta Mater.*, 2021, vol. 195, p. 113740.
32. M. Buttard, G. Martin, P. Harrison, E.F. Rauch, B. Chéhab, P. Jarry, J.J. Blandin, and P. Donnadieu: *Scripta Mater.*, 2023, vol. 226, p. 115212.
33. Y. Nie, Y.T. Chang, and M.A. Charpagne: *Acta Mater.*, 2024, vol. 275, p. 120035.
34. J.A. Eady and L.M. Hogan: *J. Cryst. Growth*, 1974, vol. 23, pp. 129–36.
35. S. Henry, G.U. Gruen, and M. Rappaz: *Metall. Mater. Trans. A*, 2004, vol. 35A, pp. 2495–2501.
36. M.A. Salgado-Ordorica, J.L. Desbiolles, and M. Rappaz: *Acta Mater.*, 2011, vol. 59, pp. 5074–84.
37. L. Yang, S. Li, X. Chang, H. Zhong, and H. Fu: *Acta Mater.*, 2015, vol. 97, pp. 269–81.
38. B. Dong, X. Cai, F. Chen, S. Lin, Y. Zong, and D. Shan: *Mater. Des.*, 2023, vol. 228, p. 111821.
39. S. Henry, P. Jarry, and M. Rappaz: *Metall. Mater. Trans. A*, 1998, vol. 29A, pp. 2807–17.